Supporting information for "Size-resolved characterizations of Fe in aerosols in East Asian outflow in winter and spring: Source apportionment and bioaccessibility"

Takuma Miyakawa[1], Chunmao Zhu[1], Morihisa Yokokawa[2], Mitsunobu Mukawa[3], Akinori Ito[1], Atsushi Shimizu[4], Tomoaki Nishizawa[4], and Yugo Kanaya[1]

[1]Research Institute for Global Change, Japan Agency for Marine-Earth Science and Technology (JAMSTEC), Yokohama, 236-0001, Japan

[2]Sibata Scientific Technology Ltd., Soka, 340-0005, Japan
[3]Murata Keisokuki Service Co. Ltd., Yokohama, 245-0052, Japan
[4]National Institute for Environmental Studies, Tsukuba, 305-8506, Japan

Correspondence to: Takuma Miyakawa (miyakawat@jamstec.go.jp)

This supporting information includes details of the custom-made shelter for PX-375 (section 1), 18 figures, and 4 tables.

S1. Custom-made shelter for PX-375

We developed a custom-made shelter for PX-375 (Horiba Ltd., Kyoto, Japan). The shelter was designed to operate the PX-375 outside of the laboratory and to conduct automated elemental composition measurements with two different size cuts which are alternately and temporally changed. The diagram of the shelter was shown in **Fig. S1a**. One sampling line (A) is vertically straight to the inlet of the PX-375 and can be used for the measurements of total suspended particulate (TSP) or aerosols with the large size cut such (e.g., PM_{10}). Another line (B) can be used for the sampling of particles with the smaller size cut, for example, PM_1 or $PM_{2.5}$., because the line was two-times bended in front of the inlet of the PX-375. The Alternate operations changing the two lines were based on the sequence of the PX-375. The PX-375 samples the ambient air using a vacuum pump for 4 hrs (step 1), then terminates the sampling (i.e., turn the pump off, step 2), then the filter roll is rotated to advance the collected particle spot to the XRF chamber (step 3), and then restart the air sampling with analyzing the samples based on the XRF technique. At steps 2–3, electric bored-through valves (AH1SR105-UUT-25, Nippon Valve Controls, Inc., Nagoya, Kapan) located upstream of the inlet of the PX-375 and behind the size cut devices were operated using a programable logic controller (KV-N14, Keyence Corp., Osaka, Japan) for changing the lines (A to B or B to A).

Theoretical penetration efficiency of aerosols particles as a function of aerodynamic diameters was calculated for line B (Hinds, 1999) and was shown in **Fig. S1c**. The results indicated the enough high penetration efficiency for the size range of the measurements of PM_1 and $PM_{2.5}$ aerosols. The biases among two lines were tested by placing the VSCCs at the upstream of lines A and B and operating the PX-375 with 2-hrs resolution alternately changing lines A and B. **Figure S2** depicted the temporal variations in $PM_{2.5}$ Sulfur, Si, and Fe mass concentrations at the headquarter of Japan Agency for Marine-Earth Science and Technology (JAMSTEC), where is located to the coastal area of Tokyo Bay and is affected by multiple

industrial emission sources (Miyakawa et al., 2020). The mass concentrations for three elements showed no systematic differences among lines for the test period. The result suggested that the use of line B for sampling $PM_{2.5}$ aerosols

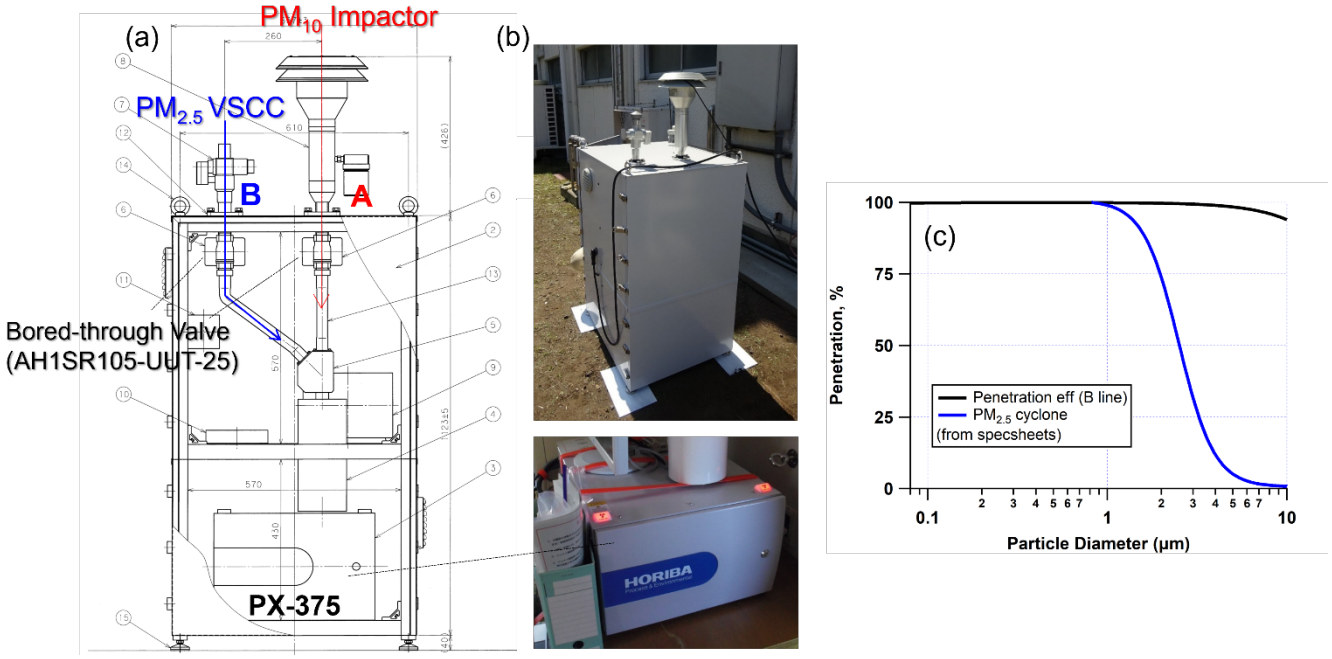

Figure S1. (a) The drawing of the custom-made shelter for the PX-375. (b) Pictures of the shelter and PX-375. (c) Theoretical penetration efficiency of aerosols for the size ranges from 0.08 to 10 μm in aerodynamic diameter with and without the very sharp cut cyclone (VSCC).

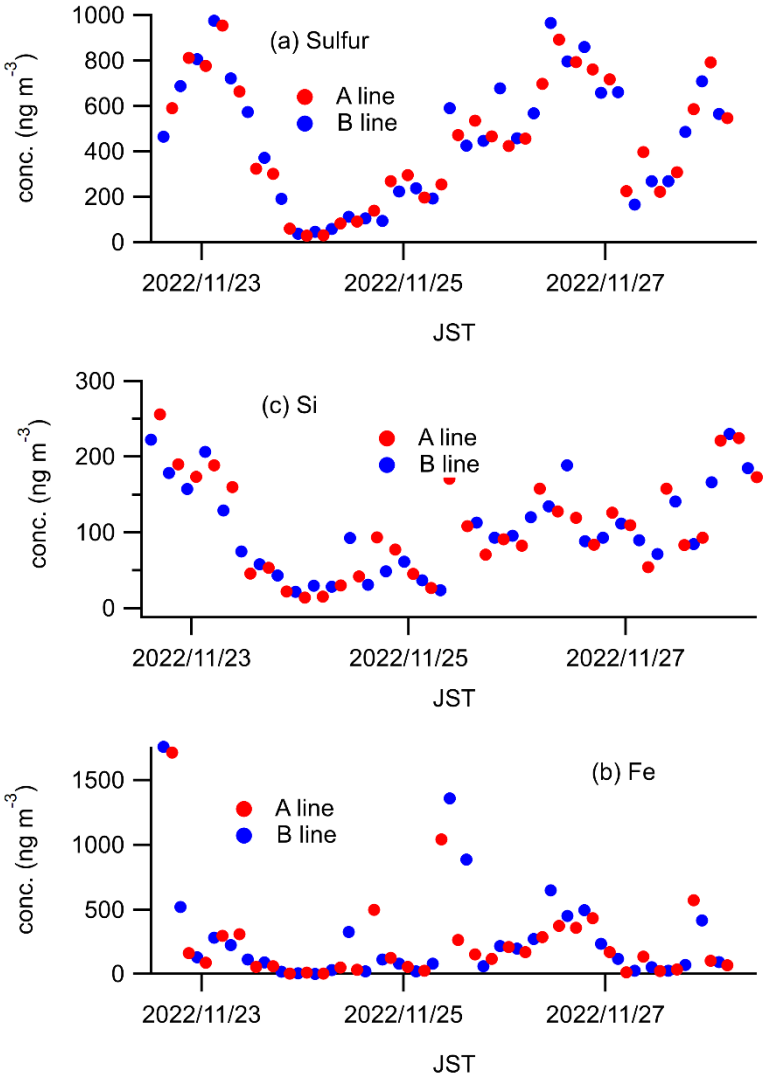

Figure S2. Temporal variations in $PM_{2.5}$ (a) Sulfur, (b) Si, and (c) Fe concentrations measured using the PX-375 changing lines A (red markers) and B (blue markers).

45

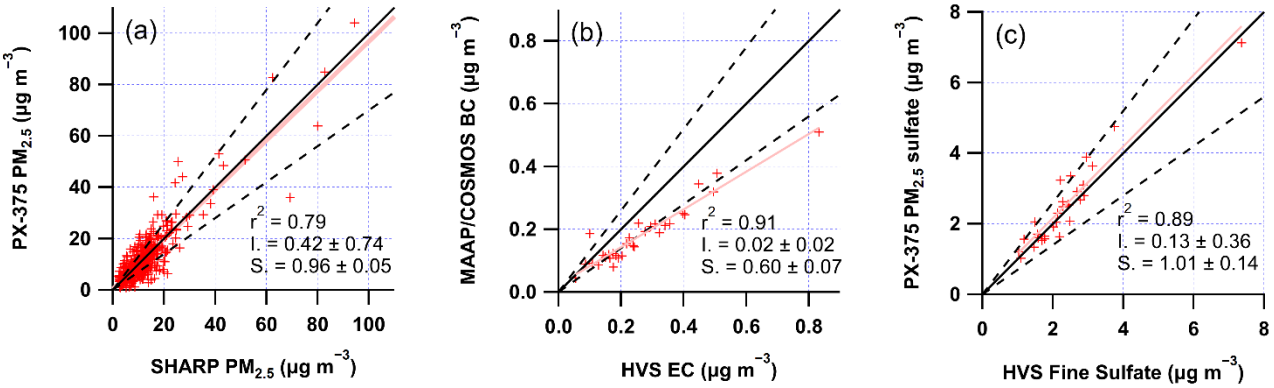

Figure S3. (a) Comparison of $PM_{2.5}$ mass concentrations between PX-375 and SHARP. (b) Comparison between MAAP/COSMOS unified BC and EC from the thermal optical analyses of the HVS samples. (c) Comparison of $PM_{2.5}$ sulfate mass concentrations between PX-375 and the chemical analyses of the HVS samples.

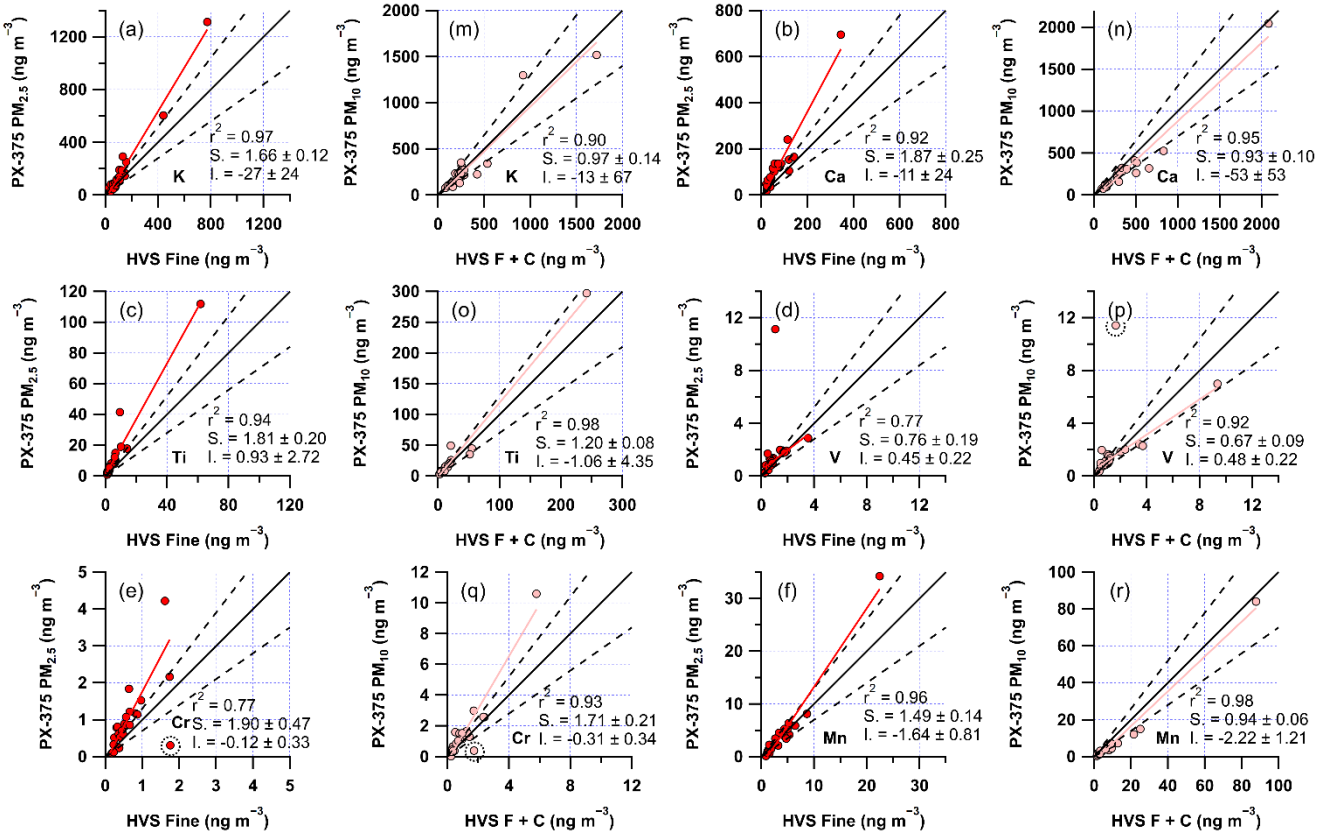

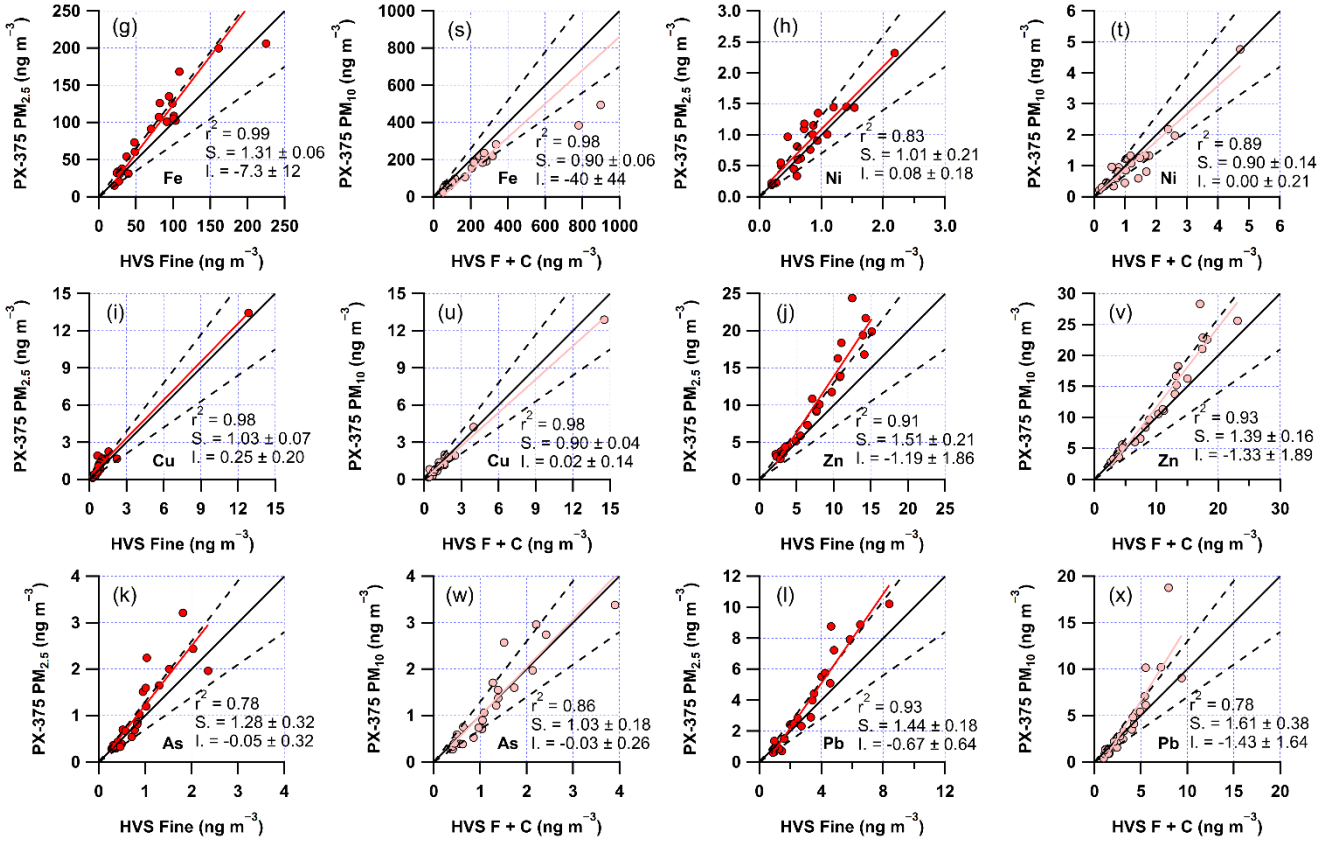

Figure S4. Comparisons of elemental concentrations measured using the PX-375 with those based on the chemical analyses of the HVS samples for K (a and m), Ca (b and n), Ti (c and o), V (d and p), Cr (e and q), Mn (f and r), Fe (g and s), Ni (h and t), Cu (i and u), Zn (j and v), As (k and w), and Pb (l and v) in $PM_{2.5}$ (red markers) and PM_{10} (pink markers) aerosols. The black solid and dashed lines depict Y = X and ±30%, respectively. The red and pink lines were the fitted lines using an orthogonal distance regression (ODR) for $PM_{2.5}$ and PM_{10} aerosols, respectively.

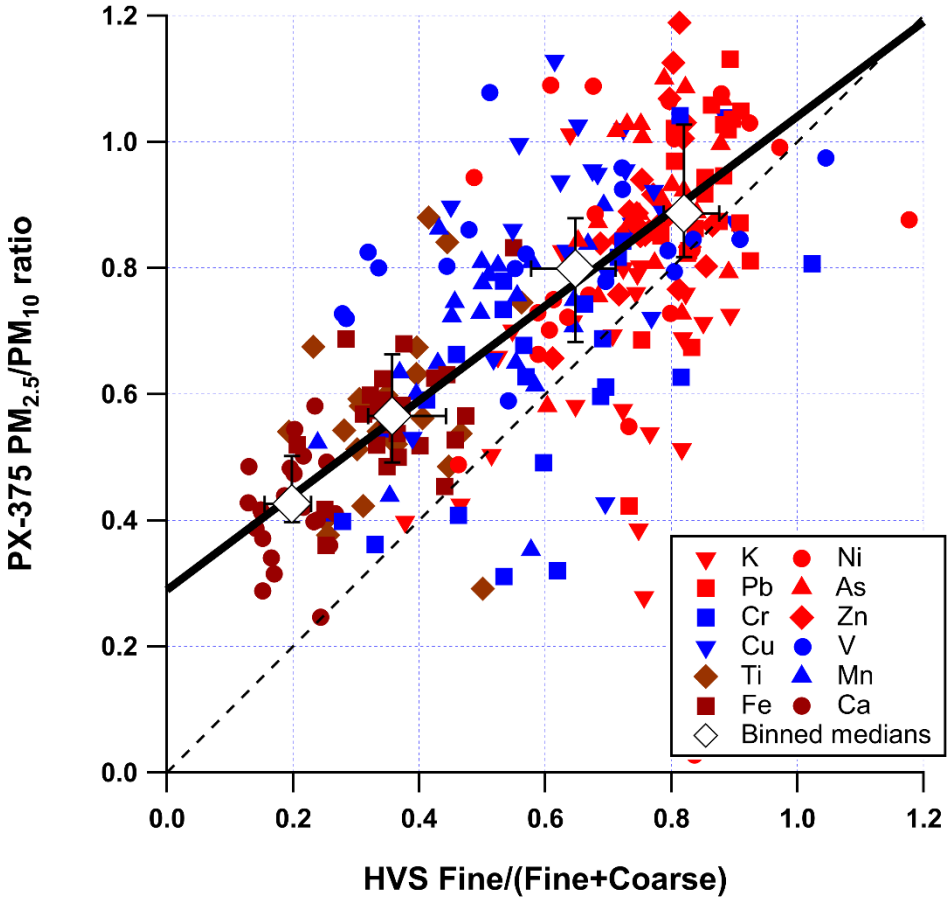

Figure S5. The relationship between PX-375-derived $PM_{2.5}/PM_{10}$ mass ratios and HVS-derived fine mode mass fraction for K (red inverse triangles), Ni (red circles), Pb (red squares), As (red triangles), Zn (red diamonds), Cr (blue squares), Cu (blue inverse triangles), V (blue circles), Mn (blue triangles), Ti (brown diamonds), Fe (brown squares), and Ca (brown circles). The binned medians were calculated for all the data points (open diamonds with error bars indicating upper and lower quartiles) and were fitted using the ODR (solid line).

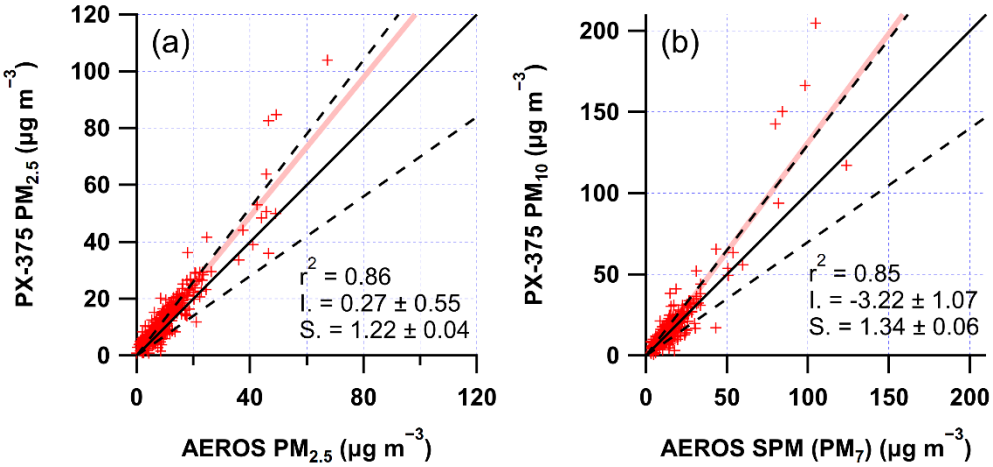

Figure S6. Comparison of (a) $PM_{2.5}$ and (b) PM_{10} aerosol mass concentrations measured using the PX-375 at the site with those at a different site (~16 km east from our site) where Ministry of Environment, Japan (MoEJ) has managed the atmospheric environmental monitoring. The black solid and dashed lines depict Y = X and ±30%, respectively. The pink lines were the fitted lines using the ODR.

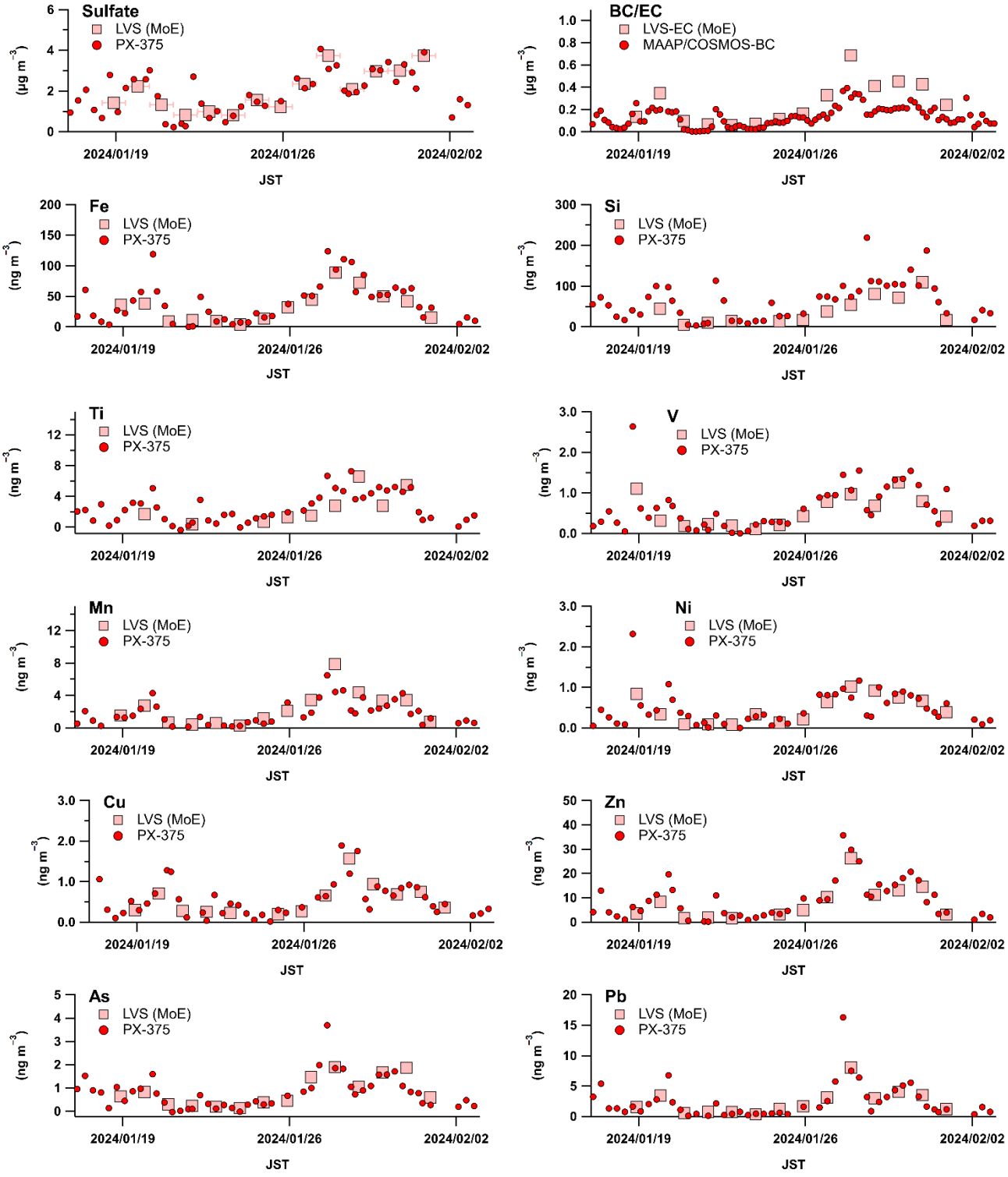
Sulfate
LVS (MoE)
PX-375
(μg m^{-3})
BC/EC
LVS-EC (MoE)
MAAP/COSMOS-BC
Fe
Si
Ti
V
Mn
Ni
Cu
Zn
As
Pb
(ng m^{-3})
2024/01/19
2024/01/26
2024/02/02
JST

Figure S7. Comparisons of temporal variations in $PM_{2.5}$ sulfate, BC/EC, Fe, Si, Ti, V, Mn, Ni, Cu, Zn, As, and Pb concentrations measured at our site (red circles) with those (pink squares) at Tamanoura site (~16.5 km south from our site) where MoEJ has managed the daily aerosol sampling using a mini-volume air sampler. The statistics of the comparison results were summarized in Table S2.

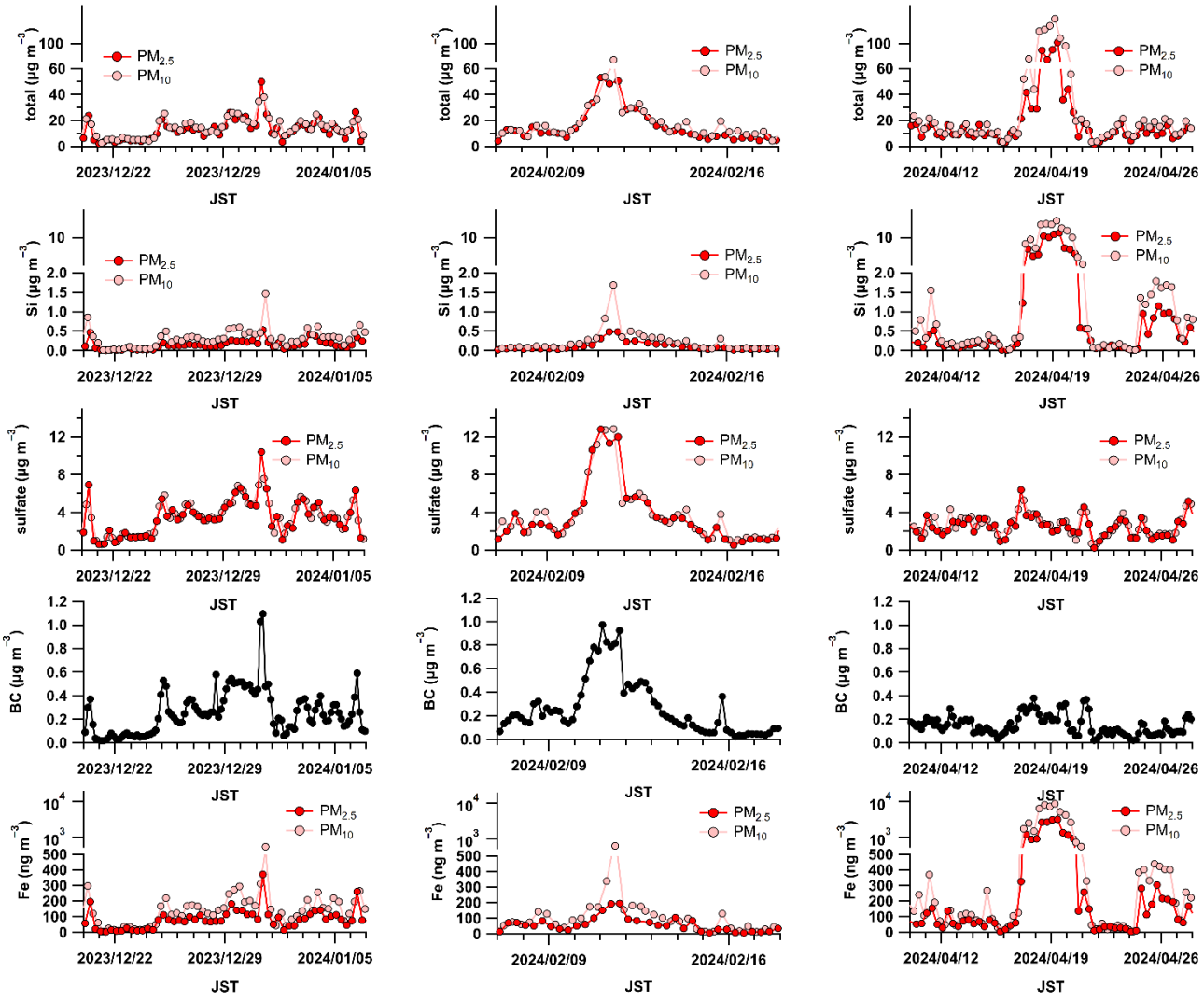

85 **Figure S8.** Example time series of aerosol concentrations of total, Si, sulfate, BC, and Fe (from top to bottom rows) for selected periods (Dec. 20, 2023–Jan. 7, 2024, Feb. 7–18, 2024 and Apr. 10–28, 2024 from left to right columns). $PM_{2.5}$ and PM_{10} data were shown as red and pink markers for total, Si, sulfate, and Fe aerosols.

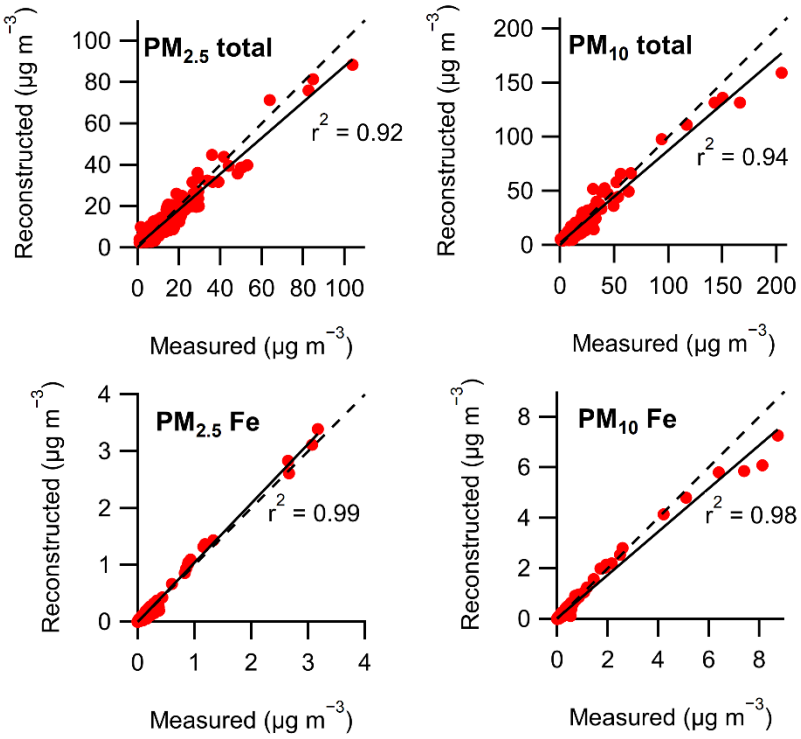

Figure S9. Correlations between reconstructed and measured $PM_{2.5}$ total, PM_{10} total, $PM_{2.5}$ Fe, and PM_{10} Fe concentrations. Dashed lines depict Y = X. The solid lines are fitting lines.

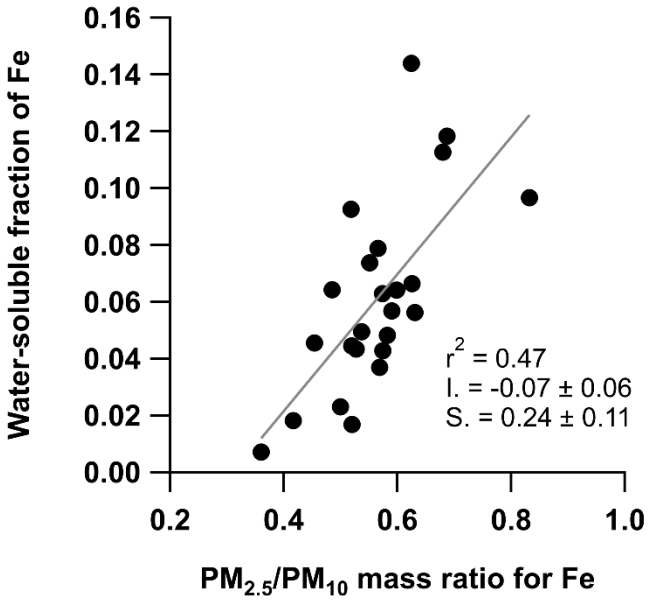

Figure S10. Relationship between water-soluble fraction of Fe ($f_{Fe,sol}$) for total (fine + coarse) aerosols and $PM_{2.5}/PM_{10}$ mass ratios of Fe. The shaded line depicts the fitting line.

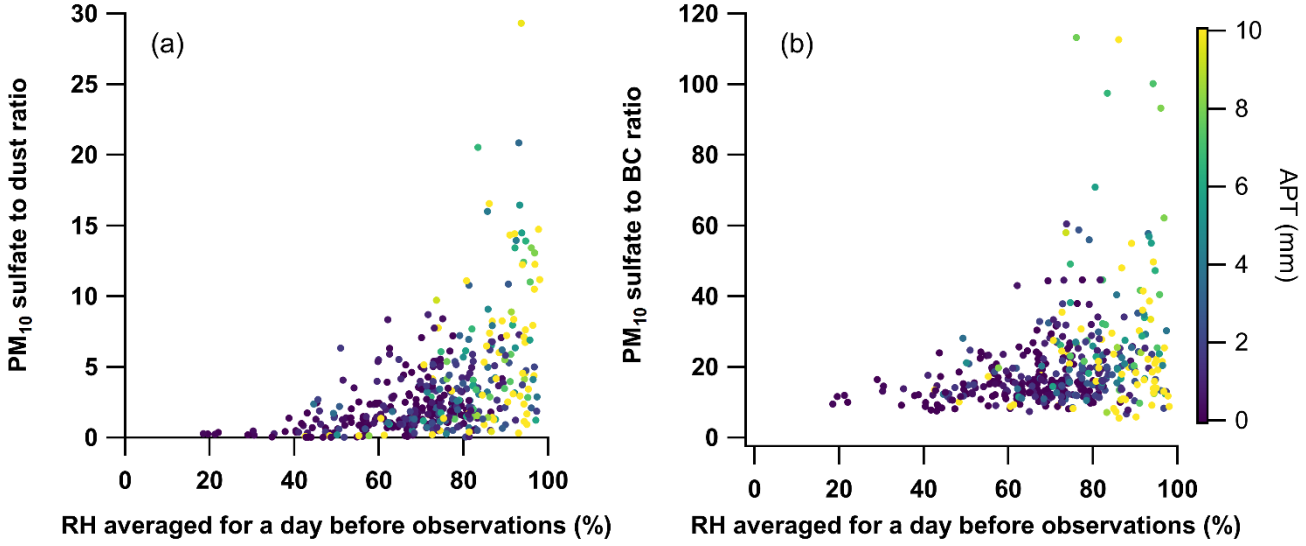

Figure S11. Changes in (a) PM_{10} sulfate/dust mass ratios and (b) PM_{10} sulfate/BC mass ratios as a function of RH averaged 1-d before the observations. The data points were colored by the accumulated precipitation along trajectories (APT).

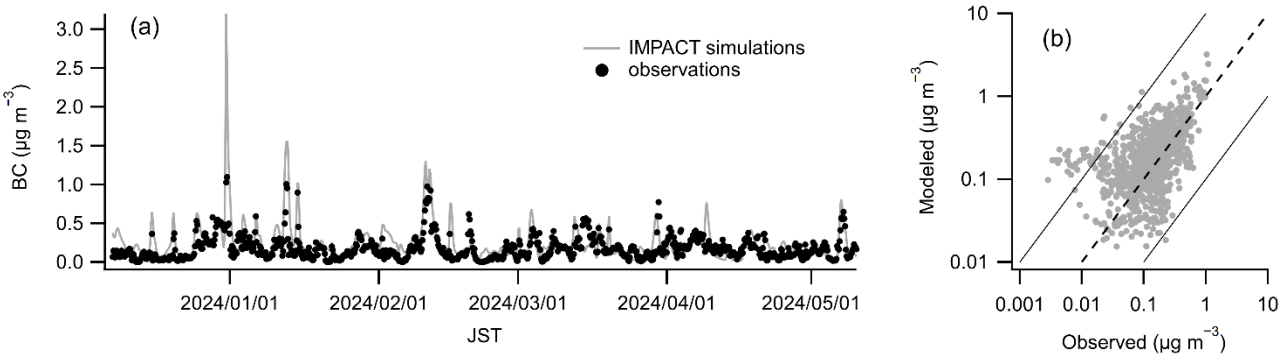

Figure S12. (a) Temporal variations in BC concentrations observed by the MAAP/COSMOS and modeled by IMPACT. (b) Correlations of BC concentrations observed by MAAP/COSMOS and modeled by IMPACT.

105

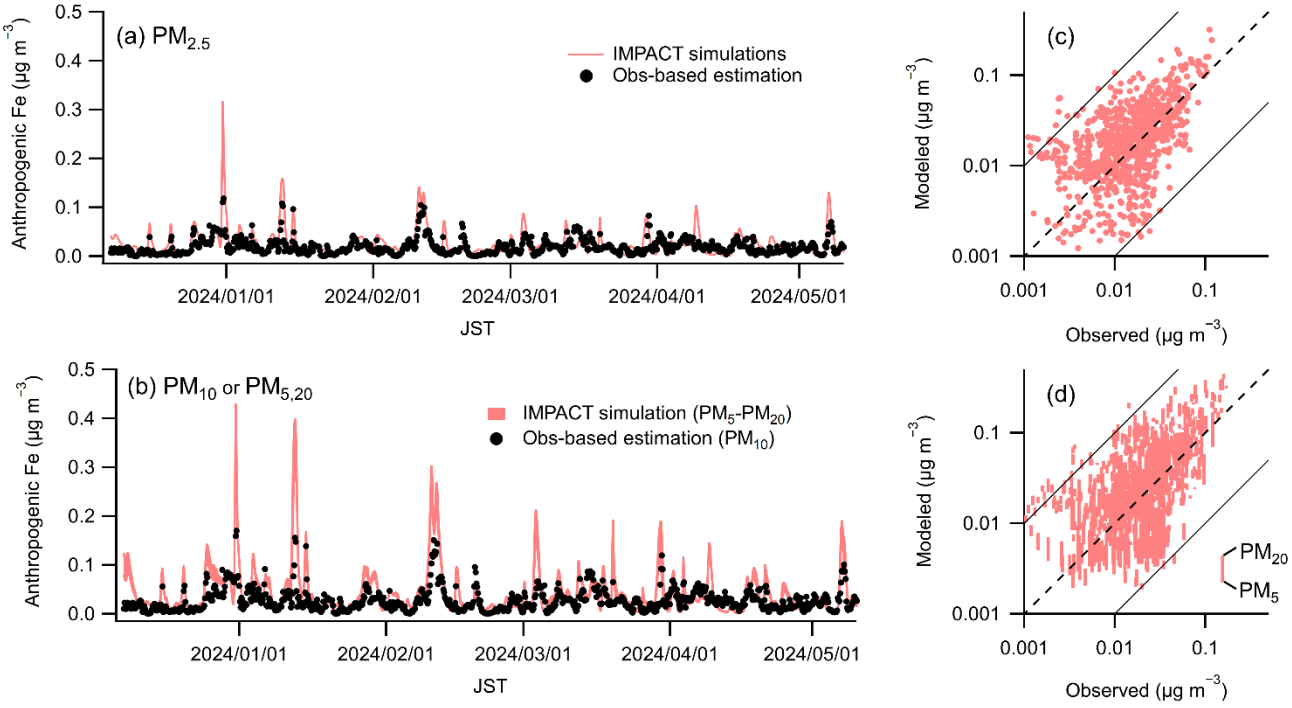

Figure S13. Temporal variations in anthropogenic Fe concentrations estimated using the MLR model and modeled by IMPACT for (a) $PM_{2.5}$ and (b) total (PM_{10} for PX-375 and PM_5 or PM_{20} for IMPACT) aerosols. Correlations of
110 anthropogenic Fe concentrations estimated using the MLR model and modeled by IMPACT for (c) $PM_{2.5}$ and (d) total (PM_{10} for PX-375 and PM_5 or PM_{20} for IMPACT) aerosols.

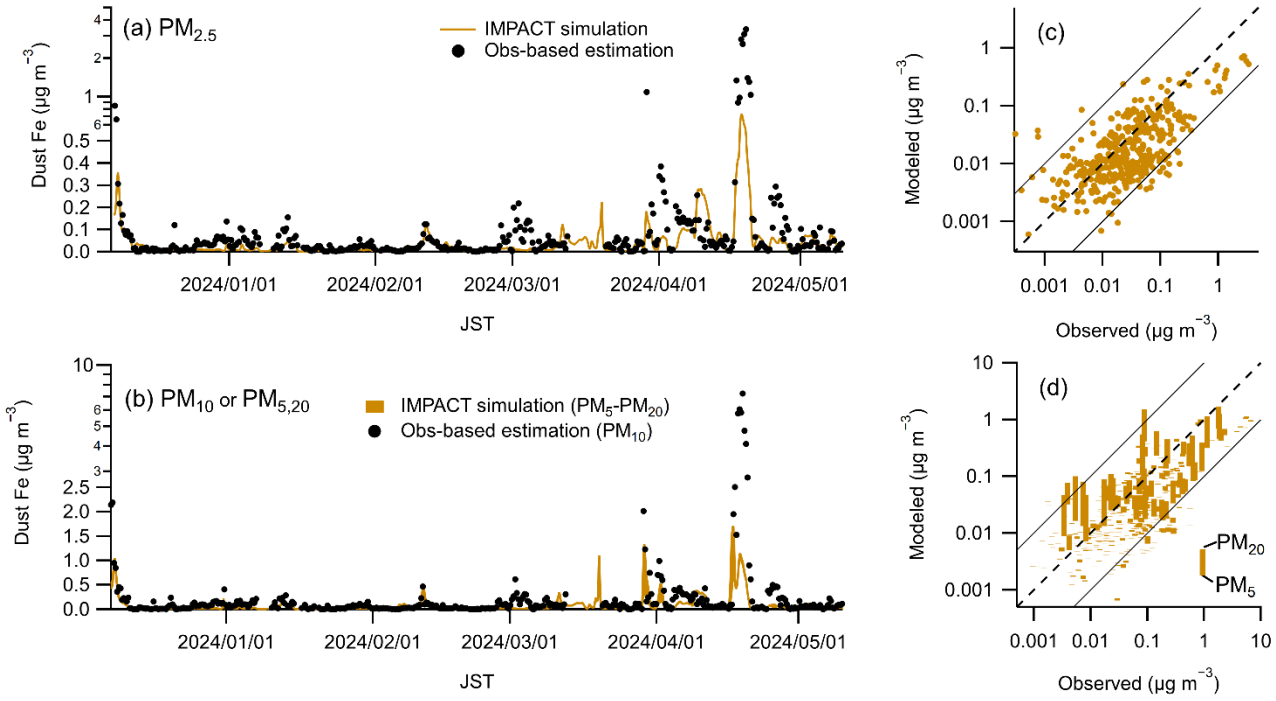

115 **Figure S14.** Temporal variations in dust Fe concentrations estimated using the MLR model and modeled by IMPACT for (a) $PM_{2.5}$ and (b) total (PM_{10} for PX-375 and PM_5 or PM_{20} for IMPACT) aerosols. Correlations of dust Fe concentrations estimated using the MLR model and modeled by IMPACT for (c) $PM_{2.5}$ and (d) total (PM_{10} for PX-375 and PM_5 or PM_{20} for IMPACT) aerosols.

120

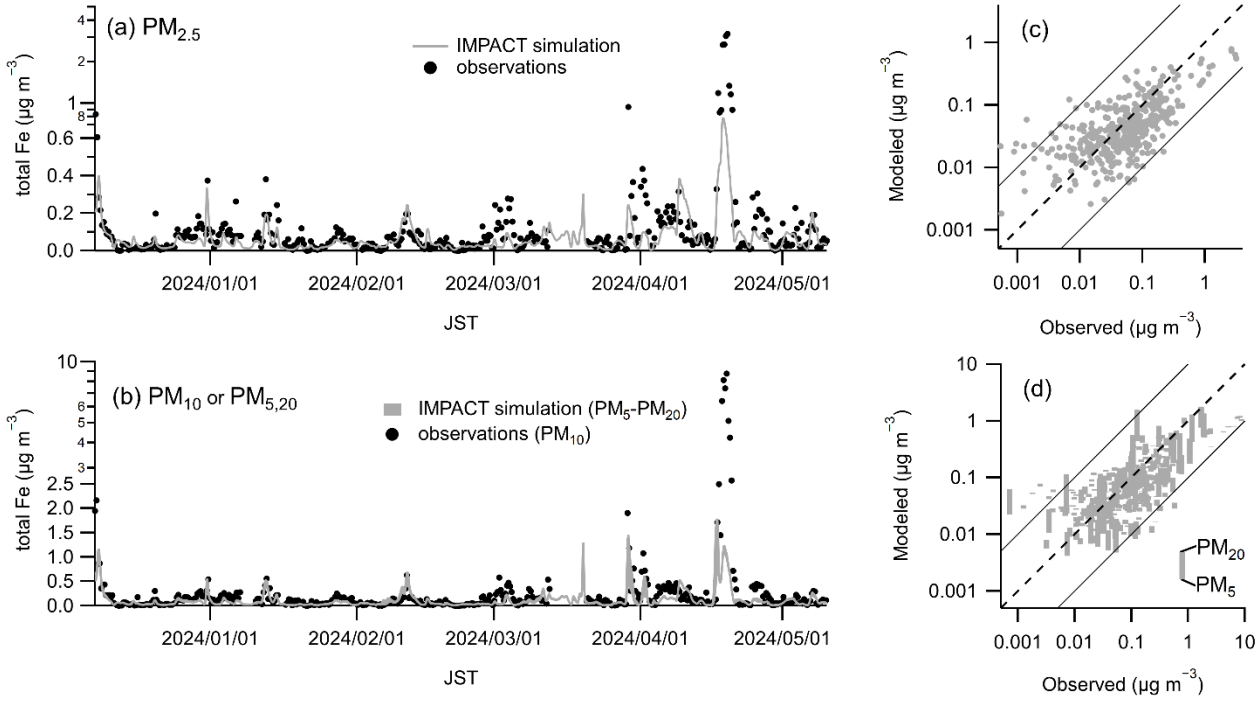

Figure S15. Temporal variations in Fe concentrations observed by the PX-375 and modeled by IMPACT for (a) $PM_{2.5}$ and (b) total (PM_{10} for PX-375 and PM_5 or PM_{20} for IMPACT) aerosols. Correlations of Fe concentrations observed by the PX-375 and modeled by IMPACT for (c) $PM_{2.5}$ and (d) total (PM_{10} for PX-375 and PM_5 or PM_{20} for IMPACT) aerosols.

125

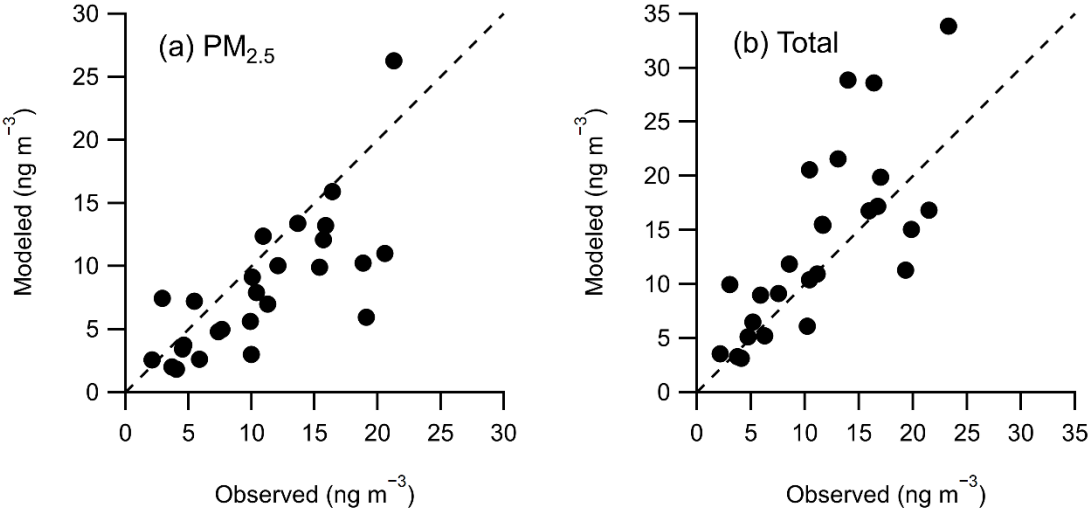

Figure S16. Correlations of measured and modeled water-soluble Fe concentrations for (a) $PM_{2.5}$ and (b) total ($PM_{2.5}$ + coarse for HVS and PM_{20} for IMPACT) aerosols.

130

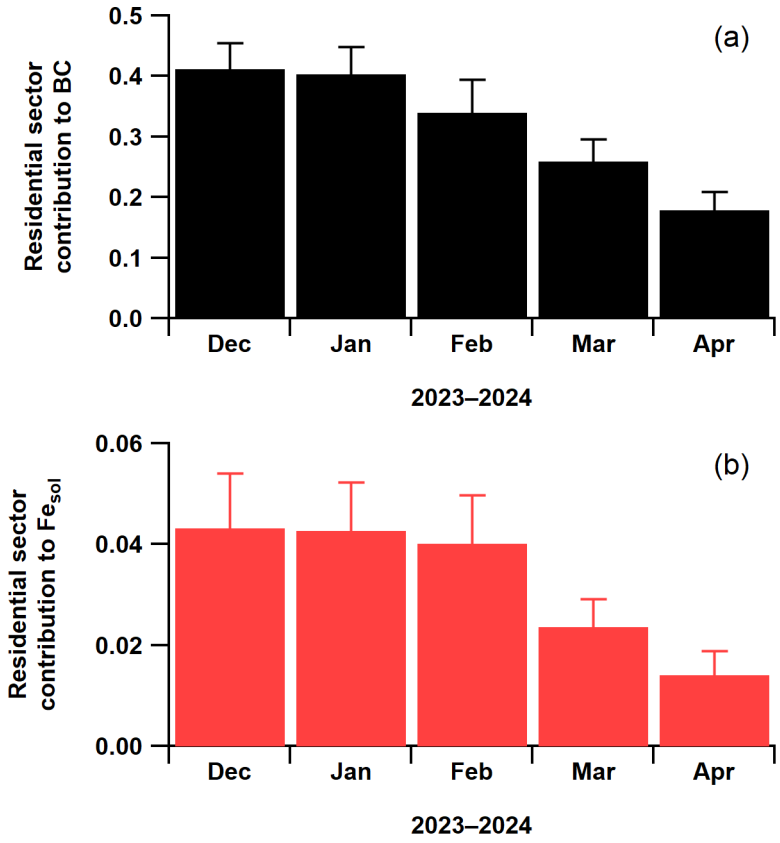

Figure S17. Monthly mean modeled residential sector contributions to (a) BC and (b) anthropogenic Fe_{sol} for PM_{20} aerosols from December 2023 to April 2024. The error bars are standard deviations.

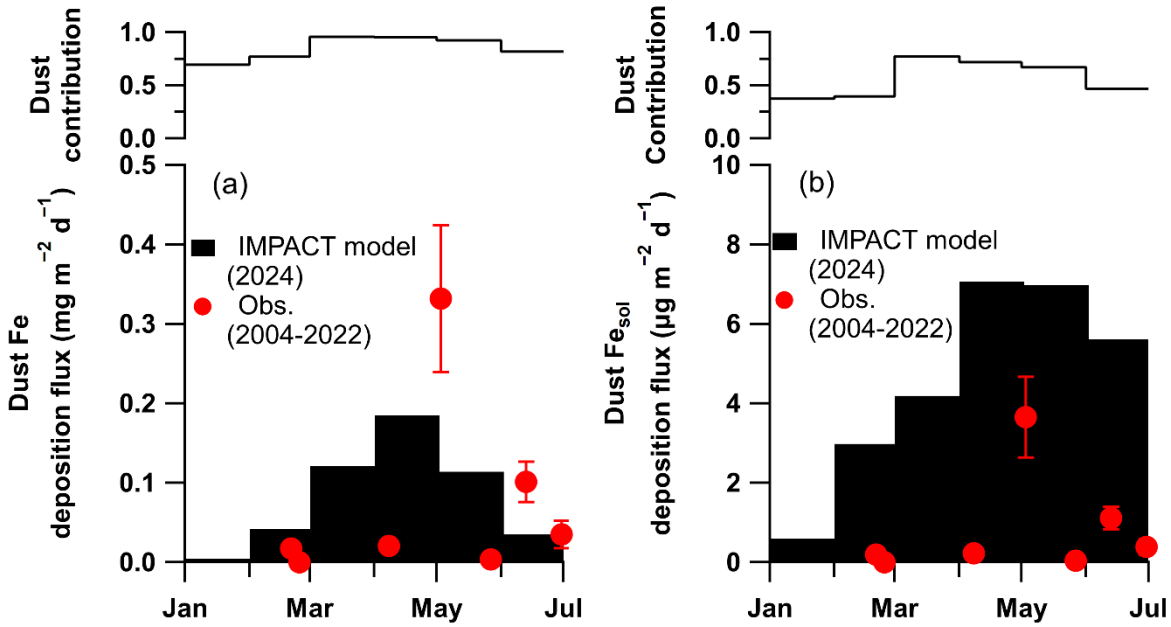

135

Figure S18. Monthly mean modeled deposition fluxes of (a) dust Fe and (b) dust Fe_{sol} for PM_{20} aerosols at an ocean observation site "K2" from January to April 2024. The observed deposition fluxes of dust Fe and Fe_{sol} at K2 during 2004–2022 (Nagashima et al., 2023) were overlayed as red markers in S18a and S18b, respectively. The upper panels in S18a and S18b depict the monthly mean dust contributions to total Fe and Fe_{sol} deposition fluxes, respectively.

140

Table S1. Summary of aerosol sampling in Fukue island using the high-volume air sampler

	Sampling start			Sampling end				Ions	Metals**	
ID	Date*	Time*	Flowrate (lpm)	Date*	Time*	Flowrate (lpm)	Volume (m3)	Fine	Fine	Coarse
fuk20_249	2023/12/2	18:24	1130	2023/12/5	11:05	1130	4534	✓	✓	✓
fuk20_250	2023/12/5	14:20	1130	2023/12/10	9:26	1130	7803	✓	✓	✓
fuk20_251	2023/12/10	9:35	1130	2023/12/15	18:48	1130	8772.2	✓	✓	✓
fuk20_252	2023/12/15	18:58	1130	2023/12/19	19:04	1130	6506.3	✓	✓	✓
fuk20_253	2023/12/19	19:13	1130	2023/12/24	15:10	1130	7881.7	✓	✓	✓
fuk20_254	2023/12/24	15:18	1130	2023/12/29	10:37	1130	7859.7	✓	✓	✓
fuk20_255	2023/12/29	10:46	1130	2024/1/3	11:20	1130	8206.6	✓	✓	✓
fuk20_256	2024/1/3	11:30	1130	2024/1/8	10:21	1130	8078.5	✓	✓	✓
fuk20_257	2024/1/8	10:35	1130	2014/1/13	18:38	1130	8741.9	✓	✓	✓
fuk20_258	2024/1/13	18:47	1130	2014/1/18	18:34	1130	8188.4	✓	✓	✓
fuk20_259	2024/1/18	18:41	1130	2024/1/22	18:26	1130	6498.6	✓		
fuk20_260	2024/1/22	18:34	1130	2024/1/27	18:18	1130	8166.8	✓		
fuk20_261	2024/1/27	18:26	1130	2024/1/31	15:01	1130	6315.1	✓		
fuk20_262	2024/1/31	15:08	1130	2024/2/4	15:01	1130	6529.1	✓		
fuk20_263	2024/2/4	15:08	1130	2024/2/9	18:39	1130	8385.9	✓	✓	✓
fuk20_264	2024/2/9	18:46	1130	2024/2/13	18:43	1130	6547.2	✓	✓	✓
fuk20_265	2024/2/13	18:51	1130	2024/2/18	10:35	1130	7614.9	✓	✓	✓
fuk20_266	2024/2/18	10:42	1130	2024/2/24	10:21	1130	9781.9	✓	✓	✓
fuk20_267	2024/2/24	10:29	1130	2024/2/28	18:29	1130	7080.7	✓	✓	✓
fuk20_268	2024/2/28	18:38	1130	2024/3/3	12:49	1130	6132	✓	✓	✓
fuk20_269	2024/3/3	12:56	1130	2024/3/8	18:24	1130	8552	✓	✓	✓
fuk20_270	2024/3/8	18:31	1130	2024/3/13	18:33	1130	8192.8	✓		
fuk20_271	2024/3/13	18:39	1130	2024/3/18	13:32	1130	7861.4	✓		
fuk20_272	2024/3/18	13:40	1130	2024/3/22	18:23	1130	6854.5	✓	✓	✓
fuk20_273	2024/3/22	18:30	1130	2024/3/27	18:23	1130	8185.9	✓	✓	✓
fuk20_274	2024/3/27	18:31	1130	2024/4/1	17:33	1130	8134.5	✓	✓	✓
fuk20_275	2024/4/1	17:41	1130	2024/4/7	10:59	1130	9351.2	✓	✓	✓
fuk20_276	2024/4/7	11:07	1130	2024/4/12	18:27	1130	8677.5	✓	✓	✓

fuk20_277	2024/4/12	18:33	1130	2024/4/17	18:24	1130	8177.5	✓	✓	✓
fuk20_278	2024/4/17	18:34	1130	2024/4/22	18:25	1130	8176	✓	✓	✓
fuk20_279	2024/4/22	18:33	1130	2024/4/28	15:22	1130	9627.4	✓	✓	✓
fuk20_280	2024/4/28	15:32	1130	2024/5/4	9:46	1130	9421.6	✓	✓	✓
fuk20_281	2024/5/4	9:54	1130	2024/5/9	18:13	1130	8742.4	✓	✓	✓

*Date and time were represented as Japanese standard time (JST = UTC + 9h).

**The samples with ID of 259-262 and 269-270 were not analyzed because the same ICP-MS used for the analyses of other samples was not available.

Table S2. Summary of aerosol sampling in Yokosuka using the high-volume air sampler

	Sampling start			Sampling end				Metals	
ID	Date*	Time*	Flowrate (lpm)	Date*	Time*	Flowrate (lpm)	Volume (m3)	Fine	Coarse
YKS22_01	2022/10/17	16:30	1133	2022/10/21	9:35	1133	6052.2	✓	✓
YKS22_02	2022/10/21	9:45	1133	2022/10/24	13:45	1133	5181.3	✓	✓
YKS22_03	2022/10/24	14:00	1133	2022/10/27	16:00	1133	5056.6	✓	✓
YKS22_04	2022/10/31	9:45	1133	2022/11/2	17:00	1133	3774.7	✓	✓
YKS22_05	2022/11/7	10:00	1133	2022/11/10	15:00	1133	5294.5	✓	✓
YKS22_06	2022/11/11	10:00	1133	2022/11/14	10:00	1133	4936.7	✓	✓
YKS22_07	2022/11/14	10:15	1133	2022/11/17	15:00	1133	5247	✓	✓
YKS22_08	2022/11/18	14:00	1133	2022/11/21	14:00	1133	4909.3	✓	✓

*Date and time was represented as Japanese standard time (UTC + 9h).

Table S3. Summary of the comparison between PX-375 and MVS

		LVS (MoEJ)[a]			PX-375[b]			
Components	Units	Avg	Std	N[c]	Avg	Std	N	r^2
Sulfate	$\mu g\ m^{-3}$	2.022	1.022	14	2.001	1.049	41	0.95
EC/BC[d]	$\mu g\ m^{-3}$	0.257	0.190	14	0.140	0.091	83	0.95
Si	$ng\ m^{-3}$	39.83	33.46	14	66.43	49.83	41	0.91
Ti	$ng\ m^{-3}$	2.589	2.140	9	2.629	1.998	41	0.59
V	$ng\ m^{-3}$	0.549	0.381	14	0.668	0.557	41	0.87
Mn	$ng\ m^{-3}$	2.350	2.084	14	1.798	1.597	41	0.83
Fe	$ng\ m^{-3}$	33.38	25.40	14	42.48	34.16	41	0.84
Ni	$ng\ m^{-3}$	0.465	0.334	14	0.508	0.441	41	0.71
Cu	$ng\ m^{-3}$	0.555	0.392	13	0.568	0.443	41	0.85
Zn	$ng\ m^{-3}$	8.023	7.141	13	9.595	8.375	41	0.95
As	$ng\ m^{-3}$	0.839	0.640	14	0.809	0.733	41	0.81
Pb	$ng\ m^{-3}$	2.383	2.057	14	2.418	3.012	41	0.96

[a]The sampling period began 10:00 of January 18, 2024 and ended 9:30 February 1, 2024 (JST).

[b]The mesruement period used for the comparison was from 08:00 of January 18, 2024 to 08:00 February 1, 2024 (JST).

[c]A Part of the data for some elements showed the below detection limits and were removed from the averaging.

[d]The offline analyses of EC performed by MOEJ were compared with the online measurements of BC at our site.

Table S4. Summary of the comparison between the observations and model simulations

Components	RMSE[a]	(units)	NMB[b]	N[c]	r^2
BC	0.20	μg m^{-3}	34.9%	929	0.42
$PM_{2.5}$ Fe	0.25	μg m^{-3}	-43.9%	423	0.66
PM_{10} Fe (vs. PM_5 and PM_{20})	0.75	μg m^{-3}	-61.6%	424	0.59
	0.74		-49.1%	424	0.39
$PM_{2.5}$ Fe_{Anth}[d]	21.5	ng m^{-3}	33.3%	929	0.45
PM_{10} Fe_{Anth} (vs. PM_5 and PM_{20})	31.8	ng m^{-3}	32.8%	929	0.48
	44.9		72.7%	929	0.47
$PM_{2.5}$ Fe_{Dust}[e]	0.26	μg m^{-3}	-57.4%	426	0.72
PM_{10} Fe_{Dust} (vs. PM_5 and PM_{20})	0.63	μg m^{-3}	-70.8%	426	0.68
	0.62		-61.0%	426	0.46
$PM_{2.5}$ Fe_{Sol}[f]	4.68	ng m^{-3}	-23.7%	26	0.56
Total[g] Fe_{Sol} (vs. PM_{20})	5.88	ng m^{-3}	21.0%	26	0.56

[a]Root mean square error
[b]Normailized mean bias
[c]Number of data points for the calculations of RMSE and MNB
[d]Fe_{Anth} stands for anthropogenic Fe.
[e]Fe_{Dust} stands for dust Fe.
[f]Fe_{sol} stands for water-soluble Fe.
[g]HVS-derived total (fine + coarse) aerosols.

References

Hinds, W. C.: Aerosol Technology: Properties, Behavior, and Measurements of Airborne Particles, 2nd ed., Wiley-Interscience Publication, 1999.

Nagashima, K., Kawakami, H., Sugie, K., Fujiki, T., Nishioka, J., Iwamoto, Y., Takemura, T., Miyakawa, T., Taketani, F., Aita, M. N.: Asian dust-deposition flux to the subarctic Pacific estimated using single quartz particles. Sci. Rep. 13, 15424, https://doi.org/10.1038/s41598-023-41201-6, 2023